HHS Public Access

Author manuscript

Neurobiol Dis. Author manuscript; available in PMC 2024 February 17.

Published in final edited form as:

Neurobiol Dis. 2023 June 15; 182: 106148. doi:10.1016/j.nbd.2023.106148.

Impaired motor unit recovery and maintenance in a knock-in mouse model of ALS-associated *Kif5a* variant

Kelly A. Rich[1], **Megan G. Pino**[1], **Mehmet E. Yalvac**[1], **Ashley Fox**[1], **Hallie Harris**[1], **Maria H. H. Balch**[1], **W. David Arnold**[2,3], **Stephen J. Kolb**[1,4]

[1]Department of Neurology, The Ohio State University Wexner Medical Center, Columbus, OH, USA

[2]NextGen Precision Health, University of Missouri, MO USA

[3]Department of Physical Medicine and Rehabilitation, University of Missouri, MO USA

[4]Department of Biological Chemistry & Pharmacology, The Ohio State University Wexner Medical Center, Columbus, OH, USA

Abstract

Kinesin family member 5A (KIF5A) is an essential, neuron-specific microtubule-associated motor protein responsible for the anterograde axonal transport of various cellular cargos. Loss of function variants in the N-terminal, microtubule-binding domain are associated with hereditary spastic paraplegia and hereditary motor neuropathy. These variants result in a loss of the ability of the mutant protein to process along microtubules. Contrastingly, gain of function splice-site variants in the C-terminal, cargo-binding domain of *KIF5A* are associated with amyotrophic lateral sclerosis (ALS), a neurodegenerative disease involving death of upper and lower motor neurons, ultimately leading to degradation of the motor unit (MU; an alpha motor neuron and all the myofibers it innervates) and death. These ALS-associated variants result in loss of autoinhibition, increased procession of the mutant protein along microtubules, and altered cargo binding. To study the molecular and cellular consequences of ALS-associated variants *in vivo*, we introduced the murine homolog of an ALS-associated *KIF5A* variant into C57BL/6 mice using CRISPR-Cas9 gene editing which produced mutant *Kif5a* mRNA and protein in neuronal tissues of heterozygous (*Kif5a*$^{+/c.3005+1G>A}$; HET) and homozygous (*Kif5a* $^{c.3005+1G>A/c.3005+1G>A}$; HOM) mice. HET and HOM mice appeared normal in behavioral and electrophysiological (compound muscle action potential [CMAP] and MU number estimation [MUNE]) outcome measures at one year of age. When subjected to sciatic nerve injury, HET and HOM mice have delayed and incomplete recovery of the MUNE compared to wildtype (WT) mice suggesting an impairment in MU repair. Moreover, aged mutant *Kif5a* mice (aged two years) had reduced MUNE independent of injury, and exacerbation of the delayed and incomplete recovery after injury compared to aged WT mice. These data suggest that ALS-associated variants may result in an impairment of the MU to respond to biological challenges such as injury and aging, leading to a failure of MU repair and maintenance. In this report, we present the behavioral,

Corresponding Author: Stephen J. Kolb, MD, PhD, 1060 Carmack Road, Rm 174, Columbus, OH 43210, Stephen.Kolb@osumc.edu.

electrophysiological and pathological characterization of mice harboring an ALS-associated *Kif5a* variant to understand the functional consequences of *KIF5A* C-terminal variants *in vivo*.

Keywords

KIF5A; ALS; motor neuron disease; peripheral nerve injury; animal model; electrophysiology

INTRODUCTION:

Axonal transport is a highly organized and precise process vital for neuronal function and, by extension, maintenance of the motor unit (MU; an alpha motor neuron and all myofibers it innervates). Kinesin family member 5A (KIF5A) is a neuron-specific cytoskeletal motor protein responsible for anterograde axonal transport of multiple cellular cargos, including neurofilaments, mitochondria, and ribonucleoproteins (Castellanos-Montiel et al., 2020; Hirokawa et al., 2009; Kanai et al., 2004, 2000; Wang and Brown, 2010). In mammals, three heavy-chain isoforms of KIF5 exist: KIF5A, KIF5B and KIF5C (Kanai et al., 2000; Miki et al., 2001). The three proteins can dimerize and, together with two kinesin light chains bound to the tail domain, form the kinesin-1 complex (Crimella et al., 2012). KIF5A has three functional domains: 1) an N-terminal motor domain responsible for microtubule binding and movement, 2) a central “stalk” domain for dimerization and interaction with other subunits, and 3) a C-terminal, cargo binding domain (Hirokawa and Noda, 2008). KIF5A has multiple cellular cargos, including neurofilaments, mitochondria and ribonucleoproteins (Castellanos-Montiel et al., 2020; Kanai et al., 2004, 2000; Wang and Brown, 2010).

Missense variants encoding the N-terminal region of *KIF5A* are associated with hereditary spastic paraplegia and Charcot-Marie-Tooth disease type 2, conditions typically involving slowly progressive motor and sensory loss and spasticity (Ebbing et al., 2008). N-terminal variants appear to result in a loss of function via a dominant negative action of mutant KIF5A on the kinesin-1 complex (Füger et al., 2012). Multiple reports suggest variants located in the C-terminal region of *KIF5A* are associated with amyotrophic lateral sclerosis (ALS) (Brenner et al., 2018; Nicolas et al., 2018). ALS-associated *KIF5A* variants are generally enriched in splice junction regions of exon 27 and result in loss of exon 27 after pre-mRNA splicing, a frameshift in exon 28, and ultimately production of an altered C-terminal cargo-binding domain (Nicolas et al., 2018). This has been shown to produce a toxic gain of function that leads to loss of autoregulation, increased propensity to form aggregates, alterations in intracellular cargo distribution, and decreased neuronal survival (Baron et al., 2022; Nakano et al., 2022; Pant et al., 2022).

KIF5A is an essential protein. *Kif5a* knockout (*Kif5a*$^{-/-}$) mice develop normally *in utero* and are alive at embryonic day 18.5, however they die shortly after birth with evidence of unexpanded lungs and failure to develop a normal breathing pattern (Karle et al., 2012; Xia et al., 2003). Conditional neuronal knockout of *Kif5a* using synapsin-promoted Cre-recombinase results in progressive hindlimb paralysis, reduced lifespan, neurofilament accumulation in neuronal soma, and loss of large caliber axons; brain levels of KIF5A in these animals were 6-to-56% of wildtype (WT) (Xia et al., 2003). In a second conditional

neuronal knockout of *Kif5a*, brain levels were 14-to-47% of WT, and no mice survived beyond four weeks (Nakajima et al., 2012).

To understand the molecular consequences of ALS-associated *KIF5A* variants *in vivo*, we created a CRISPR-Cas9 engineered mouse model carrying a C-terminal variant at the 5' splice junction of *Kif5a* exon 27 (c.3005+1G>A), homologous to an ALS-associated variant in humans (c.3020+1G>A).

MATERIALS AND METHODS

Generation of Mutant *Kif5a* Mice

Mutant *Kif5a* mice carrying an exon 27 splice junction variant (c.3005+1G>A) were created at The Ohio State University Genetically Engineered Mouse Modeling Core. All procedures were performed in accordance with NIH Guidelines and approved by the Institutional Animal Care and Use Committee (IACUC) of the Ohio State University (#2019A00000029). *Kif5a* mutant mice were created with CRISPR-Cas9 knock-in of an exon 27 splice junction variant (c.3005+1G>A) which is homologous to the ALS-associated c.3020+1 G>A variant in humans shown to result in exclusion in exon 27 (Nicolas et al., 2018). Highly-specific guide RNA (gRNA) targeting *Kif5a* exon 27, single strand donor DNA, and recombinant Hi-Fi Cas9 protein (IDT, USA) were injected into multiple WT C57BL/6 zygotes to produce the F0 founder heterozygous (*Kif5a*$^{+/c.3005+1G>A}$; HET) mice. The gRNA sequence used in this study was followed by a protospacer adjacent motif (PAM) sequence, which is a conserved part of the splice site sequence in human and mouse *Kif5a*. The introduction of the c.3005+1G>A variant destroyed the PAM sequences, thereby eliminating further cleavage of the mutated site by the Cas9 enzyme and avoided introduction of a PAM-targeting point variant in the mouse *Kif5a*, which could potentially alter mRNA splicing. This predicted novel C-terminal peptide and its human homolog caused by the c.3020+1 G>A variant are identical except for the final 13 amino acids (Figure 1A).

Sanger sequencing of the PCR product confirmed the genotype of F0 HET mice (Figure 1B). RT-PCR and Rsa1 restriction confirmed the loss of exon 27 in mRNAs from HET and HOM mice (Figure 1C). Lines were propagated by back-crossing with WT C57BL/6 mice to generate F1, F2 and F3 offspring. Homozygous (*Kif5a* $^{c.3005+1G>A/\ c.3005+1G>A}$; HOM) mice were obtained by crossing HET mice.

Mice were genotyped from tail clips using Thermo Fire isolation and PCR kits with specific primers (F:ACGATTCATGTGGACCAGCT; R:TACCCATGGGAGTGCCTGGAT). Briefly, regions ~150-basepairs (bp) upstream and downstream of *Kif5a* exon 27 were amplified and the presence of the mutant variant was confirmed by a restriction analysis using the enzyme Rsa1 to identify HET and HOM mice. Rsa1 was used because the mutation disrupts the Rsa1's cut site. After obtaining RNAs from neuronal tissues, reverse transcription PCR was performed followed by a restriction analysis using the enzyme EcoRV, which has its restriction site on exon 27. Exon 27 exclusion in HET mice was identified following restriction by the presence of three bands (one uncut and two cut bands), compared with only two cut bands found in WT mice. Sanger sequencing of the PCR products confirmed the loss of exon 27 in HET and HOM mice.

Kif5a mRNA Analysis

Euthanasia was performed by carbon dioxide inhalation followed by decapitation. Spinal cord samples (cervical/thoracic) and forebrain samples (single hemisphere, cerebellum removed) were collected in sterile 2 ml microcentrifuge tubes, flash frozen in liquid nitrogen and kept at −80°C until use. Frozen tissues were transferred to sterile 2 ml screw-cap tubes (Thermo Fisher Scientific, 15-340-162), and 600 μl of TRIzol (Invitrogen) and two 2.4 mm sterile metal beads (Thermo Fisher Scientific, 15-340-158) were added to each tube. After 5 minutes (min) at room temperature, tissues were mechanically homogenized at 6 m/s for 30 seconds (s) intervals, two times, with a 10 s pause in between (Thermo Fisher Scientific, Bead Mill-24). The resulting solutions were carefully transferred to new sterile 2 ml tubes and a standard phenol-chloroform RNA extraction was performed. Next, a DNase digest was performed (Invitrogen, AM2238). The samples were incubated on a thermocycler for 30 min at 37°C followed by a 20 min deactivation step at 80°C. The concentrations and 260/280 nm absorbance ratios were quantified using a nucleic acid spectrophotometer (Thermo Fisher Scientific, NanoDrop). RNA samples were stored at −80°C until use. First strand cDNAs were synthesized using 1 μg of template RNA, RevertAid reverse transcriptase, and random hexamer primers according to the manufacturer's instructions (RevertAid First Strand cDNA Synthesis Kit, Thermo Scientific, #K1622). Samples were diluted with 60 μl nuclease-free water and stored at −20°C until use.

mRNA expression was measured in a multiplex digital droplet PCR (ddPCR) reaction using the BioRad QX200 system. ddPCR assays were designed to specifically target exons of mouse mRNA (Supplementary Table 1). *Kif5a* expression was normalized to the constitutive *Ywhaz* tyrosine 3-monooxygenase gene. *Kif5a* exon 27 inclusion was calculated as WT *Kif5a* expression divided by total *Kif5a* expression (WT+MUT), expressed as a percent.

KIF5A Protein Analysis

Brain and spinal cord tissues were flash frozen in liquid nitrogen and kept at −80°C until use. Frozen tissues were homogenized in RIPA lysis buffer (Thermo Fisher, #89900) containing cOmplete™ protease inhibitor cocktail (Roche #04693159001) and phosphatase inhibitor cocktail (Sigma-Aldrich #P0044) and then sonicated at 2 s intervals, three times. Lysates were centrifuged at 17,000 rpm for 20 min at 4 °C and supernatants were carefully collected. Protein concentration was measured using a BCA Protein Assay Kit (Thermo Fisher, #23252, USA). Protein samples (50 μg) were run in 4–12% Bolt® Bis-Tris Plus precast 10- or 12-well polyacrylamide gels (Thermo Fisher, #NW04120BOX) and transferred to PDVF membranes (GE Healthcare, #10600021, Pittsburgh, USA). Membranes were blocked for 2 hours (h) at room temperature with 5% bovine serum albumin (BSA, Bedford, MA, USA) in Tris-Buffered Saline with 0.05% Tween-20 (TBS-T, Amresco, OH, USA) and incubated with the appropriate primary antibodies (anti-KIF5A stalk domain (rabbit α-KIF5A [1:500], Thermo Fisher PA5–29820) and anti-α tubulin (rabbit α-tubulin [1:15,000], Abcam ab7291)) in TBS-T with 5% BSA overnight at 4 °C. After washing with TBS-T for 10 min (five times) on the shaker, membranes were incubated with secondary antibody (horseradish peroxidase (HRP)-conjugated goat anti-rabbit (goat α-rabbit [1:15,000], Thermo Fisher HAF008)) in 5% dry milk in TBS-T for 1 h. Membranes were washed with TBS-T and incubated with ECL Prime western detection reagent

(Amersham, #RPN2232 NJ, USA) for 1–3 min. Chemiluminescence imaging was performed using the Azure Biosciences 600 imaging system, and band intensities were quantified using ImageJ (v. 1.51 h, NIH, Bethesda, MD, USA). The relative content of analyzed proteins in each sample was determined by normalizing band intensities to the content of α-tubulin in the same sample.

Behavioral Assessments

Grip strength, rotarod, and wire hang testing—All behavioral assessments were performed by a blinded investigator. For uninjured mice, bilateral forelimb and bilateral hindlimb grip strength (DEFII-002, Chatillon, Largo, FL, USA), rotarod (LE8205; Panlab Harvard Apparatus), and wire hang tests were performed weekly from 7 weeks (w) to 6 months of age and monthly thereafter. Body weight was recorded at all time points. To evaluate grip strength, mice were positioned parallel to the bench so that both paws (hind paws or forepaws) were allowed to grasp the bar at a time and were pulled towards the evaluator. The averages of five trials for bilateral forelimb grip strength, five trials for bilateral hindlimb grip strength, and three trials for rotarod were analyzed at each time point (maximum time of 2 min was recorded for rotarod). For longitudinal evaluations (Figure 2A), grip is presented as gram-force (gF) to accommodate both forelimb and hindlimb grip evaluations onto the same graph. Wire hang performance was reported as the longest latency to fall time out of three individual trials (maximum time of 2 min).

Unilateral hindlimb grip strength assessments were used for mice who were subject to nerve injury. Mice were positioned parallel to the bench so only the right hind paw was allowed to grasp the bar at a time and were pulled towards the evaluator. For injury and aging cohorts, grip strength was normalized to mouse weight at the time of the evaluation.

Open field testing—Mice were subjected to open field testing at 12, 18, and 24 months of age as previously described (Rice et al., 2019). Mice were kept on a 12 h light/dark cycle from 6am-6pm, and all testing occurred during the light phase. Prior to testing, mice were acclimated to the procedure room for at least 1 h. Mice were placed in the center of a square arena (40 cm ×40 cm) and locomotor activity was recorded for 10 min using a ceiling-mounted video camera (Sony Corporation, Tokyo, Japan). The apparatus was cleaned between trials using 70% ethanol. Analysis was performed using Ethovision XT 12 software (Noldus Information Technology, Wageningen, Netherlands). Assessed measures included average velocity, total distance traveled, frequency of movement, and duration of movement.

Electrophysiological Measurements

Compound muscle action potential (CMAP) of the right gastrocnemius muscle was measured following stimulation of the sciatic nerve of WT, HET and HOM mice as previously described (Arnold et al., 2015; Wier et al., 2019). Briefly, mice were anesthetized with isoflurane (3–5% for induction, 2–3% for maintenance) and the right hindlimb was shaved to allow appropriate electrode contact. An active ring electrode was placed over the gastrocnemius muscle and a reference ring electrode was placed over the metatarsals of the right hindpaw (Alpine Biomed, Skovlunde, Denmark). The skin underlying the

ring electrodes was shaved to increase contact with skin and electrode gel was used to decrease impedance (Spectra 360; Parker Laboratories, Fairfield, NJ). A common reference electrode was placed on the tail (Carefusion, Middleton, WI). Two 28-gauge monopolar needle electrodes (Teca, Oxford Instruments Medical, New York, NY) were placed on each side of the sciatic nerve in the region of the proximal thigh. A portable electrodiagnostic system (Cadwell Sierra Summit, Kennewick, WA) was used to stimulate the sciatic nerve (0.1 ms pulse, 1–10 mA intensity). CMAP baseline-to-peak amplitudes were recorded following supramaximal stimulation. Average single MU potential (SMUP) amplitude was determined by averaging the peak-to-peak amplitude differences of 10 incremental submaximal responses. MUNE was then calculated by dividing the maximum CMAP (peak-to-peak) response by the average SMUP.

Peripheral Nerve Injury

Mice were subjected to peripheral nerve injury (PNI) via sciatic nerve crush at age 14 w or 35 w. On day of surgery, mice were pre-treated with sustained-release buprenorphine (1mg/kg) and motrin (40mg/kg) and anesthetized with isoflurane (3–5% for induction, 2–3% for maintenance). Adequate depth of anesthesia was confirmed via toe pinch. The skin at the surgical site was cleaned three times with chlorhexidine and 70% ethanol. A skin and muscle incision of approximately 1 cm was then made in the posterolateral aspect of the right hindlimb to expose the sciatic nerve (Figure 4B). Prior to PNI, hemostatic forceps were dipped in carbon powder so the wound can be easily visualized during necropsy. The sciatic nerve was gently separated from the surrounding tissue and fascia and then crushed above the level of the knee using 1 mm wide hemostatic forceps to crush the nerve, with three clicks compression, two times each for 15 s, with a 15 s pause between compressions. All crush injuries were performed by a single investigator (HH). The incision was closed using 7 mm reflex wound clips (CellPoint Scientific). Animals were monitored throughout recovery and for 72 h following surgery. Reflex wound clips were removed at 10 days post-PNI.

Histopathology

Immediately following euthanasia, the sciatic nerve, gastrocnemius muscle and spinal cord were removed. Histology was performed on WT, HET, and HOM mice from young (PNI at 14 w, euthanized at 30 w) and aged (PNI at 35 w, euthanized at 100 w) cohorts to assess multiple components of the MU: motor neuron soma, axons and neuromuscular junctions (NMJs).

For spinal cord and muscle histopathology, whole tissue was immersion fixed in 4% paraformaldehyde (24 h), embedded in OCT (Tissue-Tek® O.C.T. Compound, Sakura) and stored at −80°C. 30 μm sections were cut (in 300 μm intervals) from the L3–L4 level, corresponding to the sciatic nerve motor pool (Rigaud et al., 2008), and mounted onto glass slides (Superfrost™ Plus Microscope Slides, Fisher Scientific). Sections were re-hydrated in xylene, followed by 70%, 95%, and 100% ethanol at room temperature. Slides were incubated in cresyl violet acetate buffer for 10 min at 60°C. Sections were then incubated in deionized water, 70%, 95%, and 100% ethanol, followed by xylene for 25 min. Sections were dried overnight, coverslipped (Fluoromount-G, Thermo Fisher) and imaged with light microscopy (Nikon Ti2). Neurons were identified by their location in the spinal cord (ventral

horn), size (area ≥ 200 μm^2 [Ciavarro et al., 2003]), visibly larger than interneurons and glia), clear nucleus and presence of Nissl substance arranged in polygonal clumps. ImageJ was used for motor neuron processing by a blinded evaluator (KAR) to calculate number and cross-sectional area of all motor neurons in the ventral horn (3 sections per mouse, 3 mice per genotype).

Gastrocnemius muscles were sectioned longitudinally at 50 μm, mounted onto glass slides and outlined with a hydrophobic barrier pen (Vector Laboratories). At room temperature, sections were blocked with 1% Triton-X100 and 4% goat serum in sterile PBS and washed with 1% Triton-X100 and 0.4% goat serum in sterile PBS. Sections were incubated in primary antibody for 2 h to label axons (chicken α-NF-200 [1:5000], Abcam, Ab72996) and presynaptic terminals (rabbit α-synapsin-1 [1:200], Cell Signaling, 5297S). After washing in PBS, tissues were incubated in secondary antibody (Alexa-594 goat anti-chicken [1:1000], Life Technologies, A11042; Alexa-594 goat anti-rabbit [1:1000], Invitrogen A-11012) and conjugated bungarotoxin (BTX) (α-BTX-488 [1:1000], Life Technologies, B13422) to visualize the presynaptic (axon, terminals) and postsynaptic (motor endplates of myofibers) respectively. Coverslips were sealed with Fluoromount-G. For analysis, fluorescence microscopy (Nikon Ti2) was used to image >50 *en face* NMJs per animal. Red and green channel images (individually and merged) were processed in ImageJ (v. 1.51 h, NIH, Bethesda, MD, USA). Maximum intensity projections were quantified using a custom-designed workflow (MHHB) adapted from NMJ-morph (Jones et al., 2016). NMJ innervation was graded based on colocalization of axons and motor endplates and defined by a blinded evaluator (KAR) as denervated, partially innervated or fully innervated based on existing criteria (Jones et al., 2016; Vannucci et al., 2019). Quantification of pre- and postsynaptic features of the NMJ was completed as previously described (Balch et al., 2021). Area of the nerve terminal (distal branchpoint of innervating axon and associated axon terminal branches) and acetylcholine receptor (AChR) clusters (α-bungarotoxin+) were quantified.

Sciatic nerves were fixed in 8% glutaraldehyde in phosphate buffer and processed for resin embedding as previously described (Lancaster et al., 2018). Injured sciatic nerves were dissected from the mouse, injury site was identified via visualization of the carbon powder, and a segment 5mm distal to the injury site was collected. Following glutaraldehyde fixation, nerves were incubated in 2% osmium tetroxide in phosphate buffer followed by rinses in ascending ethanol concentrations (50%, 70%, 80%, 95%, 100%) and propylene oxide. Samples were then incubated in a 1:1 propylene oxide:resin mixture and placed in resin molds, cured at 60°C for >8 h. Semi-thin sections (1 μm) were stained with alkaline toluidine blue, coverslipped using Fluoromount G (Thermo Fisher) and visualized by light microscopy (Nikon Ti2). Image quantification was performed using an automated analysis process developed in NIS-Elements AR software (v5.30) with the General Analysis 3 module (Nikon), as previously described (Simmons et al., 2021; Vetter et al., 2021). Briefly, toluidine blue-stained axons were manually identified in a training set of images covering a range of genotypes and morphology. Using the NIS-Elements module Segment.ai, a convolutional neural network was trained on these images for 1000 iterations and this network was applied to the larger cohort. Fiber number, fiber diameter (longest cross-sectional diameter measured to the outside edges of the myelin sheath), and axon diameter

(longest cross-sectional diameter measured to the inside edges of the myelin sheath) were recorded and used for statistical comparison.

For aggregation analysis, spinal cords were fixed in paraffin and a 5 μm-thick section was collected on glass slides (Superfrost™ Plus Microscope Slides, Fisher Scientific). Tissues were then deparaffinized via a stepwise incubation with the following reagents (5 min each); xylene (x3), 100% ethanol (x2), 95% ethanol (x2), 70% ethanol (x2). Slides were then transferred to a staining dish containing tris-buffered saline (TBS) and submerged in pre-heated (95°C) antigen-retrieval solution (Dako S1699) for 20 min. Slides were cooled in room-temperature dH_2O for 15 min, then washed briefly with TBS and finally PBS containing 3% H_2O_2 to block endogenous peroxidase activity (Fisher H325–500) for 15 min. A hydrophobic barrier was added and slides were incubated in TBS containing 0.1% Tween-20 (TBST). intelliPATH FLX automated slide staining system was then used to perform the following incubations; TBST (rinse), 2.5% normal horse serum (20 min), primary antibody (either rabbit anti-KIF5A [ab154414] at 5μg/mL or rabbit anti-ubiquitin [ab134953] at 0.25μg/mL, 30 min), TBST (x3, wash), immPRESS horse anti-rabbit horseradish peroxidase (Vector Laboratories (MP-7401, 30 min), TBST (x3, wash), diaminobenzidine substrate (DAB, K3468, 2.5 min), and TBST (rinse). Post-autostainer incubations included the following; dH_2O (rinse), Harris Hematoxylin (Leica 3801562, 30s), dH_2O (5x), dH_2O containing 0.1% NH_4OH (30s), dH_2O (3x), 70% ethanol (~20 dips, 1x), 95% ethanol (~20 dips, 2x), 100% ethanol (~20 dips, 3x), xylene (~20 dips, 2x). Slides were then coverslipped as described previously.

Statistical Analysis

GraphPad Prism 9 software (v9.4.1, La Jolla, CA) was used for all statistical analyses, and data were expressed as means with standard deviation (SD) for cross-sectional data or standard error of the mean (SEM) for longitudinal data. Unpaired t-test was used to compare *Kif5a* mRNA between genotypes. For open field analysis, unpaired t-tests were performed between different genotype and sex groups at single time points and paired t-tests were performed between the same group at different time points. Kaplan-Meier comparisons were used for survival analysis. One-Way ANOVA with Kruskall-Wallis test was used to compare cross-sectional behavior, electrophysiology, protein level and pathology. For all experiments, $p<0.05$ was considered significant.

RESULTS

Kif5a mutant mice exhibit normal survival and motor function

As of September 2022, >400 viable offspring have been obtained in our colony. We observed approximately Mendelian distribution between genotypes (only HET × HET crosses quantified; 22.0% WT [55.6% male and 44.4% female], 58.3% HET [47.9% male and 52.1% female] and 19.7% HOM [37.0% male, 63.0% female]). No differences in survival or weight were observed between genotypes (Figure 1D–E), nor were persistent differences observed between genotypes in our behavioral evaluations (Figure 2A–F). Of note, male mice (WT and HET) performed more poorly than female mice on rotarod (Figure 2B) and wire hang (Figure 2C). No significant differences in distance travelled

were observed between sexes or between genotypes during open field testing (Figure 2D–F; Supplementary Figure 1A–G). Taken together, these data suggest that without injury, the selected *Kif5a* variant does not decrease survival, nor does it induce an observable motor or physiological phenotype.

Kif5a WT and Δexon27 mRNA is expressed normally in spinal cord of mutant *Kif5a* mice

We quantified expression of WT and Δexon27 *Kif5a* mRNA transcripts in spinal cord tissue (Figure 3A–F) using ddPCR. Compared to WT mice, we observed a 52% reduction in WT *Kif5a* mRNA in HET mice and a 99% reduction in WT *Kif5a* mRNA in HOM mice (Figure 3B–C), confirming the expected proportional distribution of WT and Δexon27 *Kif5a* mRNA. Conversely, compared to WT mice, we observed a 36% increase in Δexon27 *Kif5a* mRNA in HET mice and a 75% increase in Δexon27 *Kif5a* mRNA in HOM mice (Figure 3D). The total amount of *Kif5a* mRNA (WT+Δexon27) did not differ between genotypes (Figure 3E–F).

Total KIF5A protein levels are reduced in neuronal tissues of HET and HOM mice

To quantify total KIF5A protein, we utilized an antibody specific for an epitope on the KIF5A stalk domain that detects both WT and Δexon27 KIF5A protein. In spinal cord, we observed a significant reduction in total KIF5A protein level in HET (55% reduction vs. WT, p=0.0016) and HOM (64% reduction vs. wildtype, p=0.0006; Figure 3G–H). There was no statistical difference between HET and HOM KIF5A protein levels (p=0.617). Similarly, in brain, we observed decreased total KIF5A protein in HET (55% reduction, p=0.004) and HOM (75% reduction, p=0.0008) compared with WT (Figure 3G, I). There were no differences in total KIF5A protein between HET and HOM (p=0.201). These findings suggest a similar reduction in KIF5A protein translation or stability in HET and HOM mice.

Impaired MUNE recovery following peripheral nerve injury in Δexon27 *Kif5a* mice

To determine whether axonal regeneration was altered in Δexon27 *Kif5a* mice, we performed weekly longitudinal assessments for 8 w post PNI (assessments began at 14 d post PNI) and again at 16 w post PNI (Figure 4A). During the first 8 w, we observed delayed MUNE recovery in HET and HOM mice as compared to WT mice (Figure 4D). Further, at 16 w post PNI, MUNE recovery, normalized to pre-injury baseline, was incomplete in HET mice (WT=1.19 vs. HET=0.68 p=0.014) and in HOM mice (WT=1.19 vs. HOM=0.61, p=0.002; Figure 4D, raw values reported in Supplementary Table 2) compared to WT mice. HET and HOM MUNE did not differ at 16 w (p=0.86). At the same timepoint, CMAP normalized to pre-injury baseline did not differ between genotypes (WT=0.90 vs. HET=0.98, p=0.79; WT=0.90 vs. HOM=0.94, p=0.94; Figure 4C, Supplementary Table 2). Unilateral hindlimb grip strength contralateral (left, Figure 4E) and ipsilateral (right, Figure 4F) to injury also did not differ between genotypes but demonstrated a slight age-related decline. As full recovery of CMAP and MUNE is expected in young animals following PNI (Giorgetti et al., 2019a), the incomplete MUNE recovery we observe in HET and HOM mice suggests a KIF5A-dependent process may be required for full recovery.

Pathological correlates of the MU following recovery from PNI in Δexon27 *Kif5a* mice

Incomplete MUNE recovery may reflect an altered function of Δexon27 KIF5A in mediating timely and complete axonal regeneration. To investigate pathological changes in individual components of the MU, we studied the neuronal soma in spinal cord, axons in sciatic nerve, and NMJs in the gastrocnemius muscle. For all pathological analyses, representative images are shown in Figure 5A.

Decreased motor neuron area in mutant mice following PNI.—At 16 w post-PNI, the number of motor neurons in the lumbar spinal cord did not differ between genotypes or sides (ipsilateral vs. contralateral; Figure 5B). No differences in average motor neuron size were observed on the contralateral side of the spinal cord (average contralateral motor neuron area: WT=814.41 μm^2, HET area=814.30 μm^2, HOM=812.62 μm^2; Figure 5C). However, ipsilateral motor neuron area was significantly decreased in HET, and further yet in HOM mice, compared to WT (average ipsilateral motor neuron area: WT=921.07 μm^2 vs. HET=749.94 μm^2, $p=0.0016$; HET vs. HOM=523.18 μm^2, $p<0.001$; Figure 5D).

Decreased sciatic nerve fiber and axon diameter in mutant mice following PNI.—The number of sciatic nerve fibers distal to the injury site did not significantly differ between genotypes for either ipsilateral nerves (average number of fibers: WT=2947, HET=3679, HOM=3646) or contralateral nerves (average number of fibers: WT=3154, HET=2797, HOM=2705; Supplementary Figure 2A). Across all genotypes, ipsilateral nerves demonstrated decreased fiber diameter (Figure 5E) and axon diameter (Figure 5F) compared to contralateral nerves. The percent difference between contralateral and ipsilateral axon and fiber diameter was greatest between WT and mutant mice (Figure 5G–H). Mean fiber diameter in the ipsilateral nerve was significantly decreased in HET vs. WT (WT=5.43 nm, HET=4.93 nm, $p<0.0001$) and smaller still in HOM vs. WT (HET=4.93 nm, HOM=4.69 nm, $p<0.0001$; Supplementary Figure 2B). Similarly, ipsilateral mean axon diameter was significantly decreased in HET vs. WT nerves (WT=3.31, HET=2.80, $p<0.0001$), though no difference in axon diameter was observed between HET and HOM (HET=2.80, HOM=2.83, $p>0.99$; Supplementary Figure 2C).

The difference between contralateral and ipsilateral mean fiber diameter was greatest in HOM mice (ipsilateral: 2.04 nm smaller, or 69.2% of contralateral diameter) followed by HET (1.39 nm, or 77.9% of contralateral) and WT (1.05 nm, or 83.7% of contralateral; Figure 5G). The difference between contralateral and ipsilateral mean axon diameter was also greatest in HOM mice (1.74 nm, or 61.2% of contralateral) followed by HET (1.45 nm, or 65.5% of contralateral) and WT (1.05 nm, or 75.8% of contralateral; Figure 5H).

Decreased pre- and post-synaptic NMJ recovery in mutant mice following PNI.—Nerve terminal area and postsynaptic (motor endplate) area did not differ across genotypes in uninjured adult animals (Supplementary Figure 4A–B). In injured mice, presynaptic nerve terminal area was significantly decreased in WT ipsilateral NMJs compared to WT contralateral NMJs (nerve terminal area in uninjured WT mice=291.42 μm^2 vs. PNI WT mice=252.26 μm^2, $p=0.0179$; Figure 5I). No differences in postsynaptic area were observed between uninjured and injured WT animals (Supplementary Figure 4E).

After recovery from PNI, ipsilateral presynaptic area was significantly decreased in HET and HOM mice compared to WT (WT=251.26 μm^2 vs. HET=129.99 μm^2, $p<0.0001$; WT vs. HOM=121.16 μm^2, $p<0.0001$; Figure 5I). HET and HOM mice also had significantly decreased ipsilateral postsynaptic area after recovery (WT=455.37 μm^2 vs. HET=318.67 μm^2, $p<0.0001$; WT vs. HOM=288.91 μm^2, $p<0.0001$; Figure 5I).

No evidence of cellular aggregation in lumbar motor neurons in WT and HET mice at baseline or after PNI—Recent studies have reported toxic aggregates in Δexon27 KIF5A models, including in vitro models (neuronal-like CAD cells, neural crest-derived N2A cells, and HEK293 cells) and in vivo models (drosophila and C. elegans) (Nakano et al., 2022; Pant et al., 2022). Ubiquitin is a common feature of cytoplasmic aggregations (Basisty et al., 2018). Across both the contralateral and ipsilateral side of post-PNI WT and HET mice, we did not observe ubiquitin-positive or KIF5A-positive granules (Supplementary Figure 5).

Aged *Kif5a* mutant mice demonstrate decreased MU maintenance

Aging is associated with a plethora of biological changes in the neuromuscular system, including a reduction in the number of functional MUs with incomplete compensatory reinnervation (Hepple and Rice, 2016; R. Deschenes, 2011; Sheth et al., 2018). Age-related decline in MU maintenance and resilience may be exacerbated by genetic variants. Indeed, the *KIF5A* disease spectrum is made up almost entirely of adult-onset conditions (Brenner et al., 2018; Crimella et al., 2012; Nicolas et al., 2018). We hypothesized that Δexon27 KIF5A may be an age-related modifier for MU maintenance in mice.

Uninjured mice of each phenotype were studied at adult (1 y) and aged (2 y) timepoints. No significant differences were observed in forelimb or hindlimb grip strength between timepoints (Figure 6A–B). With age, HET mice demonstrated a decline in MUNE compared to WT (adult HET=314.5 vs. aged HET=135.17, $p=0.0012$; Figure 6C). This was not observed at the 1-year timepoint. CMAP was maintained at each timepoint (Figure 6D).

Aged Kif5a mutant mice demonstrate diminished MU repair.—To investigate the influence of age on MU recovery following PNI, we performed PNI on WT and HET animals at an older timepoint (PNI at 35w, euthanized at 2 y). Their electrophysiological recovery was then compared to our earlier evaluations of younger mice of each genotype injured at 14 w (PNI at 14 w, euthanized at 30 w; Figure 6E–F). CMAP recovery was similar between 14 w WT, 14 w HET and 35 w WT mice, but was delayed in 35 w HET mice (Figure 6E). Interestingly, in the first few weeks following PNI, MUNE recovery was similar between 14 w HET and 35 w WT mice, both delayed compared to 14 w WT (Figure 6F). 35 w HET mice showed the most dramatic delay in MUNE recovery. These data suggest that in our model, *Kif5a* variants and age have a combined negative effect on the timing of MU recovery.

Decrease in motor neuron area exacerbated in aged mutant mice following PNI.—We evaluated motor neurons in the contralateral and ipsilateral lumbar spinal cord in adult (injured at 14 w, euthanized at 30 w) and aged animals (injured at 35 w, euthanized at

100 w) after PNI. Ipsilateral motor neuron area was decreased compared to the contralateral side only in mutant animals (Supplementary Figure 3A). The area of contralateral motor neurons was decreased in aged WT mice compared with adult WT mice but did not differ between genotypes in aged mice (Figure 6G). Ipsilateral motor neuron area in aged WT mice was significantly greater than that of aged HET mice (WT=608.44μm^2 vs. HET=450.22μm^2, p=0.002; Figure 6H). Our data suggest that motor neuron area decreases with physiological aging and this decrease is exacerbated in HET and HOM mice.

Decreased pre- and post-synaptic NMJ recovery in aged mutant mice following PNI.—We evaluated properties of the NMJ in adult (injured at 14 w, euthanized at 30 w) and aged animals (injured at 35 w, euthanized at 100 w) after PNI. Representative images are provided in Supplementary Figure 4C. Compared to injured young WT mice, nerve terminal area declined in injured aged mice, but did not differ between genotype (Figure 6I). Similar results were observed for postsynaptic area (Supplementary Figure 4E). The relative proportion of denervated NMJs increased with age, mutation status, and PNI (Supplementary Figure 4D). Our analysis suggests that aging leads to decreased pre- and postsynaptic NMJ recovery following PNI independent of genotype.

DISCUSSION

This knock-in mouse model of an ALS-associated, C-terminal variant in *Kif5a* does not have an ALS phenotype of motor neuron degeneration. This phenomenon is a perennial challenge in the ALS research field (Perrin, 2014; Stephenson and Amor, 2017). Our model differs from the most commonly used ALS models, which leverage overexpression of mutant gene products implicated in familial forms of ALS. While these models can be reliable in preclinical phenotypic progression, largely the use of overexpression models has led to limited translational benefit for ALS patients (Ludolph et al., 2010; Lutz, 2018; Philips and Rothstein, 2015). Our approach, utilizing a knock-in splice mutation, is more representative of ALS mutations found in clinical settings, however we still did not observe a phenotype independent of biological stress. Humans harboring ALS-associated KIF5A variants appear healthy for decades prior to onset of neurodegeneration, our model suggests that onset of disease in these individuals could result from accumulation of subclinical axonal stressors over time. The phenotype of altered MU repair after injury seen in this mouse model suggests individuals harboring these variants have an increased vulnerability or risk to injury and perhaps to the development or onset of neurodegeneration. MUs experience denervation, reinnervation and remodeling dynamically and must mobilize repair mechanisms repeatedly throughout life. It is notable that *KIF5A* was confirmed as an ALS-associated gene using a genome-wide association study (GWAS), and the relevance of disease association (i.e. direct causality vs. risk factor) is not always clear from this approach (Rich et al., 2021). Thus, a thorough understanding of the mechanism of impaired regeneration or maintenance in this model is still to vital to understanding the development of neurodegeneration seen in ALS, as well as to mechanisms of neuropathy and spastic paraparesis associated with loss of function *KIF5A* variants.

We observed a delayed and incomplete MU repair reflected through electrophysiological measures of MUNE and pathological correlates. Nerve regeneration is clearly impacted

by aberrations in kinesin and dynein proteins as well as in models of non-*KIF5A* CMT (Ducommun Priest et al., 2019; Shah et al., 2022; Villalón et al., 2015), however to our knowledge the work presented here represents the first evidence of MU repair deficits in ALS-associated *KIF5A* mutations. In our model, post-PNI MUs showed a holistic reduction in neuronal size at 16w post-PNI, as reflected in motor neuron soma, axons and NMJ terminals. A reduction of MUs in the setting of a CMAP recovery can be due to collateral sprouting of nerve terminals to re-innervate vacant NMJs (Arnold et al., 2015; Hepple and Rice, 2016), thereby increasing in SMUP, which is inversely proportional to MUNE (Arnold et al., 2015; Dengler et al., 1989). A post-PNI adaptation whereby motor neurons with *Kif5a* variants shrink may be related to decreased support requirements for distal segments. Loss of innervation after amputation leads to decreased motor neuron area without overt cell death (Wu and Kaas, 2000), and decreased fiber and axon diameter after PNI recovery is expected under normal conditions (Muratori et al., 2012). As such, exacerbation of these decreases in our injured HET and HOM mice suggests that ΔExon27 KIF5A may alter cellular distribution of cargos (e.g. neurofilament) necessary for full fiber and axon recovery (Yuan et al., 2017). In the extreme case of absence of KIF5A in conditional *Kif5a*$^{-/-}$ mice, there is clear neurofilament accumulation in dorsal root ganglia (Xia et al., 2003). Thus, it is possible that after PNI HET and HOM mice undergo relative loss of capacity for neurofilament transport, thus explaining the loss of neuronal volume.

In a recent study, denervation of the facial nerve via PNI was shown to lead to short-term declines in nerve terminal area and long-term adaptive NMJ reorganization with recovery of synaptic function (Bermedo-García et al., 2022). The long-term defect in NMJ reorganization observed in our injured HET and HOM mice suggests diminished ability to transport neurotrophic support factors or differences in neuronal signaling, ultimately leading to problems with presynaptic NMJ reformation (Gordon, 2020). We suspect that there is loss of a transport capacity and that, at least during axonal repair, becomes limiting for normal recovery. Transport failure of KIF5A has been identified as a key cause of retinal ganglion cell neurodegeneration after optic nerve injury using an unbiased, quantitative analysis of the proteome after nerve crush (Shah et al., 2022). After injury, transportomic analysis showed reductions in KIF5A protein levels as well as proteins involved in cytoskeletal maintenance and protein synthesis. These findings support the notion that a decrease in axonal transport capacity may be occurring in our model system.

KIF5A protein expression levels were, indeed, reduced in the spinal cord and brain of HET and HOM mice, despite no reduction in mRNA levels across genotypes. Therefore, while the ALS-associated variant successfully altered splicing with loss of exon 27, we find no evidence of nonsense mediated decay or other RNA processing alteration *in vivo*. The reduction of total soluble KIF5A protein suggests that there is either an impairment of translation, increase in turnover or formation of insoluble aggregates. KIF5A does appear to be more aggregate-prone than other kinesin-1 isoforms (Chiba et al., 2022). While the protein level of WT and ΔExon27 KIF5A are equal in RIPA-soluble fraction, ΔExon27 KIF5A is found at a much higher concentration in urea-soluble fractions toxicity (Pant et al., 2022). Recent *in vitro* analysis has shown that WT KIF5A will oligomerize with ΔExon27 KIF5A, which leads to aggregates in neurites and ultimately neural toxicity (Nakano et al., 2022; Pant et al., 2022). Aggregates are also seen in microtubule mechanosensory neurons

in *C. elegans* models of ΔExon27 where the mutant protein is overexpressed relative to WT levels of KIF5A (Nakano et al., 2022). Our histological approach did not identify visible aggregates in contralateral or ipsilateral motor neurons of WT and HET mice following PNI. This finding may reflect differences between cell types studied, location of aggregates (cell soma vs. neurites), and/or our phenotype simply being too mild to induce aggregation. Regardless, these findings, in the context of the inherent differences between transgenic and knock-in models of ALS, raises the possibility that overexpression-specific effects may account for aggregation findings in previous models.

Studies of kinesin function *in vitro* show that Δexon27 has a toxic gain of function with the WT allele and alters normal autoinhibition, resulting in an increased rate of procession down microtubules (Baron et al., 2022; Nakano et al., 2022; Pant et al., 2022). This would be predicted to result in an accumulation of kinesin-1 in the presynaptic terminal of the NMJ. We did not observe this in our *in vivo* model; however, it is possible that loss of autoinhibition also results in aggregation and/or targeting for protein degradation.

Links between cellular changes in aging and those associated with adult-onset neurodegeneration are increasingly appreciated (Azam et al., 2021; Wyss-Coray, 2016). In laboratory models of ALS, markers of premature aging (e.g., synaptic input loss, signaling abnormalities, mitochondrial aberrations) have been reported (Herskovits et al., 2018; Kreiter et al., 2018; Pandya and Patani, 2020). Moreover, hallmarks of aging such as reduced telomere activity and altered metabolic profiles in cells derived from patients with ALS suggest shared mechanisms (De Felice et al., 2014; Gerou et al., 2021). We observed accelerated loss of MU in aged mutant mice relative to aged WT controls and impaired MUNE recovery after PNI. These results suggest that ALS-associated variants may lead to defects in MU maintenance and repair. MUNE declines with natural aging and following recovery from PNI (Giorgetti et al., 2019b; Sheth et al., 2018) due to collateral sprouting of nerve terminals to re-innervate vacant NMJs as well as increased size of surviving MUs (Hepple and Rice, 2016). Loss of MU also occurs in humans during natural aging, accompanied by motor neuron loss (Piasecki et al., 2016). In addition, aged nerves regenerate at a slower pace than young nerves for a host of reasons, including delayed Wallerian degeneration, decreased availability of trophic factors, and decline in transport of cytoskeletal proteins (Kawabuchi et al., 2011). Premature aging of the MU may occur with Δexon27 KIF5A, ultimately placing additional biological strain on MUs in aging and, to a greater extent, PNI.

The molecular consequences of Δexon27 KIF5A expression that led to ALS onset is likely to include increased protein aggregation, reduced autoinhibition and alteration of the protein sequence of the cargo binding domain. In our model, mouse Δexon27 *Kif5a* expression leads to an overall decrease in soluble protein expression. A limitation of this model is that the resultant C-terminal peptide sequence of the mouse Δexon27 KIF5A is not identical to that of the human Δexon27 KIF5A. The terminal amino acids differ although the biophysical properties of the two sequences appear to be similar (hydrophobicity 30.17 [human] vs. 28.88 [mouse], isoelectric point 9.0 vs 9.0; Thermo Fisher Scientific Peptide Synthesis and Proteotypic Peptide Analyzing Tool). Therefore, changes in axonal contents reported in human iPS cell-derived Δexon27 KIF5A neurons may not be reflected precisely in this

mouse model. Nevertheless, this model could serve as an important system to validate findings in human-derived cell lines.

An unexpected finding was that HOM mice are apparently normal, even though there is no wildtype Kif5a mRNA or protein present, unless there is an insult and need for increased axonal transport capacity. Thus, in mice, alterations to the cargo binding domain due to loss of exon27 are well tolerated, similar to observations in individuals with *KIF5A*-associated ALS until disease onset in adulthood. We interpret the phenotype of impaired MU repair in this model to be related more to the overall reduction in the availability of soluble KIF5A than to specific alterations in cargo binding. We suggest that the adult onset of ALS in individuals with *KIF5A* variants may stem from a reduction in overall KIF5A availability throughout life, rather than from specific changes in molecular cargos. Future work in these mice is warranted to test potential therapies aimed at correction of exon 27 exclusion and to identify alterations in axonal contents during MU repair.

Supplementary Material

Refer to Web version on PubMed Central for supplementary material.

Acknowledgements:

The authors would like to acknowledge Anthony Brown, PhD, Paul Monsma, PhD, Anthony Vetter, PhD, Shari Dunaway, MD and Mithu De, PhD for their technical and intellectual contributions to this manuscript. We also thank Arthur Burghes, PhD and his lab for use of their ddPCR equipment and their technical contributions, as well as Chen Gu, PhD and his lab for use of their open field-testing equipment and analysis software. We are grateful for the funding support of the following sources: the Julie Bonasera Fund for ALS and Neuromuscular Diseases, the William White Family Fund for ALS, Ohio State Neurological Institute and NIH R03NS116303 (to SJK).

REFERENCES:

Arnold WD, Sheth KA, Wier CG, Kissel JT, Burghes AH, Kolb SJ, 2015. Electrophysiological Motor Unit Number Estimation (MUNE) Measuring Compound Muscle Action Potential (CMAP) in Mouse Hindlimb Muscles. J. Vis. Exp. JoVE 10.3791/52899

Azam S, Haque Md.E., Balakrishnan R, Kim I-S, Choi D-K, 2021. The Ageing Brain: Molecular and Cellular Basis of Neurodegeneration. Front. Cell Dev. Biol 9, 683459. 10.3389/fcell.2021.683459 [PubMed: 34485280]

Balch MHH, Harris H, Chugh D, Gnyawali S, Rink C, Nimjee SM, Arnold WD, 2021. Ischemic stroke-induced polyaxonal innervation at the neuromuscular junction is attenuated by robot-assisted mechanical therapy. Exp. Neurol 343, 113767. 10.1016/j.expneurol.2021.113767 [PubMed: 34044000]

Baron DM, Fenton AR, Saez-Atienzar S, Giampetruzzi A, Sreeram A, Shankaracharya, Keagle PJ, Doocy VR, Smith NJ, Danielson EW, Andresano M, McCormack MC, Garcia J, Bercier V, Van Den Bosch L, Brent JR, Fallini C, Traynor BJ, Holzbaur ELF, Landers JE, 2022. ALS-associated KIF5A mutations abolish autoinhibition resulting in a toxic gain of function. Cell Rep. 39, 110598. 10.1016/j.celrep.2022.110598 [PubMed: 35385738]

Basisty N, Schilling B, Rabinovitch PS, 2018. Identifying ubiquitinated proteins and aggregates. Aging 10, 2549–2550. 10.18632/aging.101605 [PubMed: 30335616]

Bermedo-García F, Zelada D, Martínez E, Tabares L, Henríquez JP, 2022. Functional regeneration of the murine neuromuscular synapse relies on long-lasting morphological adaptations. BMC Biol. 20, 158. 10.1186/s12915-022-01358-4 [PubMed: 35804361]

Brenner D, Yilmaz R, Müller K, Grehl T, Petri S, Meyer T, Grosskreutz J, Weydt P, Ruf W, Neuwirth C, Weber M, Pinto S, Claeys KG, Schrank B, Jordan B, Knehr A, Günther K, Hübers A, Zeller D,

Kubisch C, Jablonka S, Sendtner M, Klopstock T, de Carvalho M, Sperfeld A, Borck G, Volk AE, Dorst J, Weis J, Otto M, Schuster J, Del Tredici K, Braak H, Danzer KM, Freischmidt A, Meitinger T, Strom TM, Ludolph AC, Andersen PM, Weishaupt JH, The German ALS network MND-NET, Weyen U, Hermann A, Hagenacker T, Koch JC, Lingor P, Göricke B, Zierz S, Baum P, Wolf J, Winkler A, Young P, Bogdahn U, Prudlo J, Kassubek J, 2018. Hot-spot KIF5A mutations cause familial ALS. Brain 141, 688–697. 10.1093/brain/awx370 [PubMed: 29342275]

Castellanos-Montiel MJ, Chaineau M, Durcan TM, 2020. The Neglected Genes of ALS: Cytoskeletal Dynamics Impact Synaptic Degeneration in ALS. Front. Cell. Neurosci 14. 10.3389/fncel.2020.594975

Chiba K, Ori-McKenney KM, Niwa S, McKenney RJ, 2022. Synergistic autoinhibition and activation mechanisms control kinesin-1 motor activity. Cell Rep. 39, 110900. 10.1016/j.celrep.2022.110900 [PubMed: 35649356]

Ciavarro GL, Calvaresi N, Botturi A, Bendotti C, Andreoni G, Pedotti A, 2003. The densitometric physical fractionator for counting neuronal populations: application to a mouse model of familial amyotrophic lateral sclerosis. J. Neurosci. Methods 129, 61–71. 10.1016/s0165-0270(03)00201-2 [PubMed: 12951233]

Crimella C, Baschirotto C, Arnoldi A, Tonelli A, Tenderini E, Airoldi G, Martinuzzi A, Trabacca A, Losito L, Scarlato M, Benedetti S, Scarpini E, Spinicci G, Bresolin N, Bassi M, 2012. Mutations in the motor and stalk domains of KIF5A in spastic paraplegia type 10 and in axonal Charcot-Marie-Tooth type 2. Clin. Genet 82, 157–164. 10.1111/j.1399-0004.2011.01717.x [PubMed: 21623771]

De Felice B, Annunziata A, Fiorentino G, Manfellotto F, D'Alessandro R, Marino R, Borra M, Biffali E, 2014. Telomerase expression in amyotrophic lateral sclerosis (ALS) patients. J. Hum. Genet 59, 555–561. 10.1038/jhg.2014.72 [PubMed: 25142509]

Dengler R, Konstanzer A, Hesse S, Schubert M, Wolf W, 1989. Collateral nerve sprouting and twitch forces of single motor units in conditions with partial denervation in man. Neurosci. Lett 97, 118–122. 10.1016/0304-3940(89)90149-3 [PubMed: 2918993]

Ducommun Priest M, Navarro MF, Bremer J, Granato M, 2019. Dynein promotes sustained axonal growth and Schwann cell remodeling early during peripheral nerve regeneration. PLOS Genet. 15, e1007982. 10.1371/journal.pgen.1007982 [PubMed: 30779743]

Ebbing B, Mann K, Starosta A, Jaud J, Schöls L, Schüle R, Woehlke G, 2008. Effect of spastic paraplegia mutations in KIF5A kinesin on transport activity. Hum. Mol. Genet 17, 1245–1252. 10.1093/hmg/ddn014 [PubMed: 18203753]

Füger P, Sreekumar V, Schüle R, Kern JV, Stanchev DT, Schneider CD, Karle KN, Daub KJ, Siegert VK, Flötenmeyer M, Schwarz H, Schöls L, Rasse TM, 2012. Spastic paraplegia mutation N256S in the neuronal microtubule motor KIF5A disrupts axonal transport in a Drosophila HSP model. PLoS Genet. 8, e1003066. 10.1371/journal.pgen.1003066 [PubMed: 23209432]

Gerou M, Hall B, Woof R, Allsop J, Kolb SJ, Meyer K, Shaw PJ, Allen SP, 2021. Amyotrophic lateral sclerosis alters the metabolic aging profile in patient derived fibroblasts. Neurobiol. Aging 105, 64–77. 10.1016/j.neurobiolaging.2021.04.013 [PubMed: 34044197]

Giorgetti E, Obrecht M, Ronco M, Panesar M, Lambert C, Accart N, Doelemeyer A, Nash M, Bidinosti M, Beckmann N, 2019a. Magnetic Resonance Imaging as a Biomarker in Rodent Peripheral Nerve Injury Models Reveals an Age-Related Impairment of Nerve Regeneration. Sci. Rep 9, 13508. 10.1038/s41598-019-49850-2 [PubMed: 31534149]

Giorgetti E, Panesar M, Zhang Y, Joller S, Ronco M, Obrecht M, Lambert C, Accart N, Beckmann N, Doelemeyer A, Perrot L, Fruh I, Mueller M, Pierrel E, Summermatter S, Bidinosti M, Shimshek DR, Brachat S, Nash M, 2019b. Modulation of Microglia by Voluntary Exercise or CSF1R Inhibition Prevents Age-Related Loss of Functional Motor Units. Cell Rep. 29, 1539–1554.e7. 10.1016/j.celrep.2019.10.003 [PubMed: 31693894]

Gordon T, 2020. Peripheral Nerve Regeneration and Muscle Reinnervation. Int. J. Mol. Sci 21, E8652. 10.3390/ijms21228652

Hepple RT, Rice CL, 2016. Innervation and neuromuscular control in ageing skeletal muscle: Innervation and neuromuscular control in ageing skeletal muscle. J. Physiol 594, 1965–1978. 10.1113/JP270561 [PubMed: 26437581]

Herskovits AZ, Hunter TA, Maxwell N, Pereira K, Whittaker CA, Valdez G, Guarente LP, 2018. SIRT1 deacetylase in aging-induced neuromuscular degeneration and amyotrophic lateral sclerosis. Aging Cell 17, e12839. 10.1111/acel.12839 [PubMed: 30295421]

Hirokawa N, Noda Y, 2008. Intracellular Transport and Kinesin Superfamily Proteins, KIFs: Structure, Function, and Dynamics. Physiol. Rev 10.1152/physrev.00023.2007

Jones RA, Reich CD, Dissanayake KN, Kristmundsdottir F, Findlater GS, Ribchester RR, Simmen MW, Gillingwater TH, 2016. NMJ-morph reveals principal components of synaptic morphology influencing structure–function relationships at the neuromuscular junction. Open Biol. 6, 160240. 10.1098/rsob.160240 [PubMed: 27927794]

Kanai Y, Dohmae N, Hirokawa N, 2004. Kinesin transports RNA: isolation and characterization of an RNA-transporting granule. Neuron 43, 513–525. 10.1016/j.neuron.2004.07.022 [PubMed: 15312650]

Kanai Y, Okada Y, Tanaka Y, Harada A, Terada S, Hirokawa N, 2000. KIF5C, a novel neuronal kinesin enriched in motor neurons. J. Neurosci. Off. J. Soc. Neurosci 20, 6374–6384.

Karle KN, Möckel D, Reid E, Schöls L, 2012. Axonal transport deficit in a KIF5A(−/−) mouse model. Neurogenetics 13, 169–179. 10.1007/s10048-012-0324-y [PubMed: 22466687]

Kawabuchi M, Tan H, Wang S, 2011. Age affects reciprocal cellular interactions in neuromuscular synapses following peripheral nerve injury. Ageing Res. Rev 10, 43–53. 10.1016/j.arr.2010.10.003 [PubMed: 20943206]

Kreiter N, Pal A, Lojewski X, Corcia P, Naujock M, Reinhardt P, Sterneckert J, Petri S, Wegner F, Storch A, Hermann A, 2018. Age-dependent neurodegeneration and organelle transport deficiencies in mutant TDP43 patient-derived neurons are independent of TDP43 aggregation. Neurobiol. Dis 115, 167–181. 10.1016/j.nbd.2018.03.010 [PubMed: 29630989]

Lancaster E, Li J, Hanania T, Liem R, Scheideler MA, Scherer SS, 2018. Myelinated axons fail to develop properly in a genetically authentic mouse model of Charcot-Marie-Tooth disease type 2E. Exp. Neurol 308, 13–25. 10.1016/j.expneurol.2018.06.010 [PubMed: 29940160]

Ludolph AC, Bendotti C, Blaugrund E, Chio A, Greensmith L, Loeffler J-P, Mead R, Niessen HG, Petri S, Pradat P-F, Robberecht W, Ruegg M, Schwalenstöcker B, Stiller D, van den Berg L, Vieira F, von Horsten S, 2010. Guidelines for preclinical animal research in ALS/MND: A consensus meeting. Amyotroph. Lateral Scler. Off. Publ. World Fed. Neurol. Res. Group Mot. Neuron Dis 11, 38–45. 10.3109/17482960903545334

Lutz C, 2018. Mouse models of ALS: Past, present and future. Brain Res. 1693, 1–10. 10.1016/j.brainres.2018.03.024 [PubMed: 29577886]

Miki H, Setou M, Kaneshiro K, Hirokawa N, 2001. All kinesin superfamily protein, KIF, genes in mouse and human. Proc. Natl. Acad. Sci. U. S. A 98, 7004–7011. 10.1073/pnas.111145398 [PubMed: 11416179]

Muratori L, Ronchi G, Raimondo S, Giacobini-Robecchi MG, Fornaro M, Geuna S, 2012. Can regenerated nerve fibers return to normal size? A long-term post-traumatic study of the rat median nerve crush injury model. Microsurgery 32, 383–387. 10.1002/micr.21969 [PubMed: 22434492]

Nakajima K, Yin X, Takei Y, Seog D-H, Homma N, Hirokawa N, 2012. Molecular motor KIF5A is essential for GABA(A) receptor transport, and KIF5A deletion causes epilepsy. Neuron 76, 945–961. 10.1016/j.neuron.2012.10.012 [PubMed: 23217743]

Nakano J, Chiba K, Niwa S, 2022. An ALS -associated KIF5A mutant forms oligomers and aggregates and induces neuronal toxicity. Genes Cells 27, 421–435. 10.1111/gtc.12936 [PubMed: 35430760]

Nicolas A, Kenna K, Renton AE, Ticozzi N, Faghri F, Chia R, Dominov JA, Kenna BJ, Nalls MA, Keagle P, Rivera AM, van Rheenen W, Murphy NA, van Vugt JJFA, Geiger JT, van der Spek R, Pliner HA,Shankaracharya, Smith BN, Marangi G, Topp SD, Abramzon Y, Gkazi AS, Eicher JD, Kenna A, Logullo FO, Simone I, Logroscino G, Salvi F, Bartolomei I, Borghero G, Murru MR, Costantino E, Pani C, Puddu R, Caredda C, Piras V, Tranquilli S, Cuccu S, Corongiu D, Melis M, Milia A, Marrosu F, Marrosu MG, Floris G, Cannas A, Capasso M, Caponnetto C, Mancardi G, Origone P, Mandich P, Conforti FL, Cavallaro S, Mora G, Marinou K, Sideri R, Penco S, Mosca L, Lunetta C, Pinter GL, Corbo M, Riva N, Carrera P, Volanti P, Mandrioli J, Fini N, Fasano A, Tremolizzo L, Arosio A, Ferrarese C, Trojsi F, Tedeschi G, Monsurrò MR, Piccirillo G, Femiano C, Ticca A, Ortu E, La Bella V, Spataro R, Colletti T, Sabatelli M, Zollino M, Conte A, Luigetti M, Lattante S, Santarelli M, Petrucci A, Pugliatti M, Pirisi A, Parish LD, Occhineri P, Giannini

F, Battistini S, Ricci C, Benigni M, Cau TB, Loi D, Calvo A, Moglia C, Brunetti M, Barberis M, Restagno G, Casale F, Marrali G, Fuda G, Ossola I, Cammarosano S, Canosa A, Ilardi A, Manera U, Grassano M, Tanel R, Pisano F, Mazzini L, Messina S, D'Alfonso S, Corrado L, Ferrucci L, Harms MB, Goldstein DB, Shneider NA, Goutman S, Simmons Z, Miller TM, Chandran S, Pal S, Manousakis G, Appel S, Simpson E, Wang L, Baloh RH, Gibson S, Bedlack RS, Lacomis D, Sareen D, Sherman A, Bruijn L, Penny M, Moreno C, de AM, Kamalakaran S, Allen AS, Boone BE, Brown R, Carulli JP, Chesi A, Chung WK, Cirulli ET, Cooper GM, Couthouis J, Day-Williams AG, Dion PA, Gitler AD, Glass J, Han Y, Harris T, Hayes SD, Jones AL, Keebler J, Krueger BJ, Lasseigne BN, Levy SE, Lu YF, Maniatis T, McKenna-Yasek D, Myers RM, Petrovski S, Pulst SM, Raphael AR, Ravits J, Ren Z, Rouleau GA, Sapp PC, Sims KB, Staropoli JF, Waite LL, Wang Q, Wimbish JR, Xin WW, Phatnani H, Kwan J, Broach JR, Arcila-Londono X, Lee EB, Van Deerlin VM, Fraenkel E, Ostrow LW, Baas F, Zaitlen N, Berry JD, Malaspina A, Fratta P, Cox GA, Thompson LM, Finkbeiner S, Dardiotis E, Hornstein E, MacGowan DJ, Heiman-Patterson T, Hammell MG, Patsopoulos NA, Dubnau J, Nath A, Musunuri RL, Evani US, Abhyankar A, Zody MC, Kaye J, Wyman S, LeNail A, Lima L, Rothstein JD, Svendsen CN, Van Eyk J, Maragakis NJ, Kolb SJ, Cudkowicz M, Baxi E, Benatar M, Taylor JP, Wu G, Rampersaud E, Wuu J, Rademakers R, Züchner S, Schule R, McCauley J, Hussain S, Cooley A, Wallace M, Clayman C, Barohn R, Statland J, Swenson A, Jackson C, Trivedi J, Khan S, Katz J, Jenkins L, Burns T, Gwathmey K, Caress J, McMillan C, Elman L, Pioro E, Heckmann J, So Y, Walk D, Maiser S, Zhang J, Silani V, Gellera C, Ratti A, Taroni F, Lauria G, Verde F, Fogh I, Tiloca C, Comi GP, Sorarù G, Cereda C, De Marchi F, Corti S, Ceroni M, Siciliano G, Filosto M, Inghilleri M, Peverelli S, Colombrita C, Poletti B, Maderna L, Del Bo R, Gagliardi S, Querin G, Bertolin C, Pensato V, Castellotti B, Camu W, Mouzat K, Lumbroso S, Corcia P, Meininger V, Besson G, Lagrange E, Clavelou P, Guy N, Couratier P, Vourch P, Danel V, Bernard E, Lemasson G, Laaksovirta H, Myllykangas L, Jansson L, Valori M, Ealing J, Hamdalla H, Rollinson S, Pickering-Brown S, Orrell RW, Sidle KC, Hardy J, Singleton AB, Johnson JO, Arepalli S, Polak M, Asress S, Al-Sarraj S, King A, Troakes C, Vance C, de Belleroche J, ten Asbroek ALMA, Muñoz-Blanco JL, Hernandez DG, Ding J, Gibbs JR, Scholz SW, Floeter MK, Campbell RH, Landi F, Bowser R, Kirby J, Pamphlett R, Gerhard G, Dunckley TL, Brady CB, Kowall NW, Troncoso JC, Le Ber I, Heiman-Patterson TD, Kamel F, Van Den Bosch L, Strom TM, Meitinger T, Shatunov A, van Eijk K, de Carvalho M, Kooyman M, Middelkoop B, Moisse M, McLaughlin R, van Es M, Weber M, Boylan KB, Van Blitterswijk M, Morrison K, Basak AN, Mora JS, Drory V, Shaw P, Turner MR, Talbot K, Hardiman O, Williams KL, Fifita JA, Nicholson GA, Blair IP, Esteban-Pérez J, García-Redondo A, Al-Chalabi A, Al Kheifat A, Andersen P, Chio A, Cooper-Knock J, Dekker A, Redondo AG, Gotkine M, Hide W, Iacoangeli A, Kiernan M, Landers J, Mill J, Neto MM, Pardina JM, Newhouse S, Pinto S, Pulit S, Robberecht W, Shaw C, Sproviero W, Tazelaar G, van Damme P, van den Berg L, van Vugt J, Veldink J, Zatz M, Bauer DC, Twine NA, Rogaeva E, Zinman L, Brice A, Feldman EL, Ludolph AC, Weishaupt JH, Trojanowski JQ, Stone DJ, Tienari P, Chiò A, Shaw CE, Traynor BJ, 2018. Genome-wide Analyses Identify KIF5A as a Novel ALS Gene. Neuron 97, 1268–1283.e6. 10.1016/j.neuron.2018.02.027 [PubMed: 29566793]

Pandya VA, Patani R, 2020. Decoding the relationship between ageing and amyotrophic lateral sclerosis: a cellular perspective. Brain 143, 1057–1072. 10.1093/brain/awz360 [PubMed: 31851317]

Pant DC, Parameswaran J, Rao L, Loss I, Chilukuri G, Parlato R, Shi L, Glass JD, Bassell GJ, Koch P, Yilmaz R, Weishaupt JH, Gennerich A, Jiang J, 2022. ALS-linked KIF5A ΔExon27 mutant causes neuronal toxicity through gain-of-function. EMBO Rep. 23, e54234. 10.15252/embr.202154234 [PubMed: 35735139]

Perrin S, 2014. Preclinical research: Make mouse studies work. Nature 507, 423–425. 10.1038/507423a [PubMed: 24678540]

Philips T, Rothstein JD, 2015. Rodent Models of Amyotrophic Lateral Sclerosis. Curr. Protoc. Pharmacol 69, 5.67.1–5.67.21. 10.1002/0471141755.ph0567s69

Piasecki M, Ireland A, Jones DA, McPhee JS, 2016. Age-dependent motor unit remodelling in human limb muscles. Biogerontology 17, 485–496. 10.1007/s10522-015-9627-3 [PubMed: 26667009]

Deschenes MR, 2011. Motor Unit and Neuromuscular Junction Remodeling with Aging. Curr. Aging Sci 4, 209–220. 10.2174/1874609811104030209 [PubMed: 21529328]

Rice J, Coutellier L, Weiner JL, Gu C, 2019. Region-specific interneuron demyelination and heightened anxiety-like behavior induced by adolescent binge alcohol treatment. Acta Neuropathol. Commun 7, 173. 10.1186/s40478-019-0829-9 [PubMed: 31703603]

Rich KA, Roggenbuck J, Kolb SJ, 2021. Searching Far and Genome-Wide: The Relevance of Association Studies in Amyotrophic Lateral Sclerosis. Front. Neurosci 14, 603023. 10.3389/fnins.2020.603023 [PubMed: 33584177]

Rigaud M, Gemes G, Barabas M-E, Chernoff DI, Abram SE, Stucky CL, Hogan QH, 2008. Species and strain differences in rodent sciatic nerve anatomy: implications for studies of neuropathic pain. Pain 136, 188–201. 10.1016/j.pain.2008.01.016 [PubMed: 18316160]

Shah SH, Schiapparelli LM, Ma Y, Yokota S, Atkins M, Xia X, Cameron EG, Huang T, Saturday S, Sun CB, Knasel C, Blackshaw S, Yates JR, Cline HT, Goldberg JL, 2022. Quantitative transportomics identifies Kif5a as a major regulator of neurodegeneration. eLife 11, e68148. 10.7554/eLife.68148 [PubMed: 35259089]

Sheth KA, Iyer CC, Wier CG, Crum AE, Bratasz A, Kolb SJ, Clark BC, Burghes AHM, Arnold WD, 2018. Muscle strength and size are associated with motor unit connectivity in aged mice. Neurobiol. Aging 67, 128–136. 10.1016/j.neurobiolaging.2018.03.016 [PubMed: 29656012]

Simmons TR, Vetter TA, Huang N, Vulin-Chaffiol A, Wein N, Flanigan KM, 2021. Pre-clinical dose-escalation studies establish a therapeutic range for U7snRNA-mediated DMD exon 2 skipping. Mol. Ther. - Methods Clin. Dev 21, 325–340. 10.1016/j.omtm.2021.03.014 [PubMed: 33898631]

Stephenson J, Amor S, 2017. Modelling amyotrophic lateral sclerosis in mice. Drug Discov. Today Dis. Models 25–26, 35–44. 10.1016/j.ddmod.2018.10.001

Vannucci B, Santosa KB, Keane AM, Jablonka-Shariff A, Lu C-Y, Yan Y, MacEwan M, Snyder-Warwick AK, 2019. What is Normal? Neuromuscular junction reinnervation after nerve injury. Muscle Nerve 60, 604–612. 10.1002/mus.26654 [PubMed: 31408210]

Vetter TA, Nicolau S, Bradley AJ, Frair EC, Flanigan KM, 2021. Automated immunofluorescence analysis for sensitive and precise dystrophin quantification in muscle biopsies. Neuropathol. Appl. Neurobiol nan.12785. 10.1111/nan.12785

Villalón E, Dale JM, Jones M, Shen H, Garcia ML, 2015. Exacerbation of Charcot-Marie-Tooth type 2E neuropathy following traumatic nerve injury. Brain Res. 1627, 143–153. 10.1016/j.brainres.2015.09.024 [PubMed: 26423936]

Wang L, Brown A, 2010. A hereditary spastic paraplegia mutation in kinesin-1A/KIF5A disrupts neurofilament transport. Mol. Neurodegener 5, 52. 10.1186/1750-1326-5-52 [PubMed: 21087519]

Wier CG, Crum AE, Reynolds AB, Iyer CC, Chugh D, Palettas MS, Heilman PL, Kline DM, Arnold WD, Kolb SJ, 2019. Muscle contractility dysfunction precedes loss of motor unit connectivity in SOD1(G93A) mice. Muscle Nerve 59, 254–262. 10.1002/mus.26365 [PubMed: 30370671]

Wu CW, Kaas JH, 2000. Spinal cord atrophy and reorganization of motoneuron connections following long-standing limb loss in primates. Neuron 28, 967–978. 10.1016/s0896-6273(00)00167-7 [PubMed: 11163280]

Wyss-Coray T, 2016. Ageing, neurodegeneration and brain rejuvenation. Nature 539, 180–186. 10.1038/nature20411 [PubMed: 27830812]

Xia C-H, Roberts EA, Her L-S, Liu X, Williams DS, Cleveland DW, Goldstein LSB, 2003. Abnormal neurofilament transport caused by targeted disruption of neuronal kinesin heavy chain KIF5A. J. Cell Biol 161, 55–66. 10.1083/jcb.200301026 [PubMed: 12682084]

Yuan A, Rao MV, Veeranna, null, Nixon RA, 2017. Neurofilaments and Neurofilament Proteins in Health and Disease. Cold Spring Harb. Perspect. Biol 9. 10.1101/cshperspect.a018309

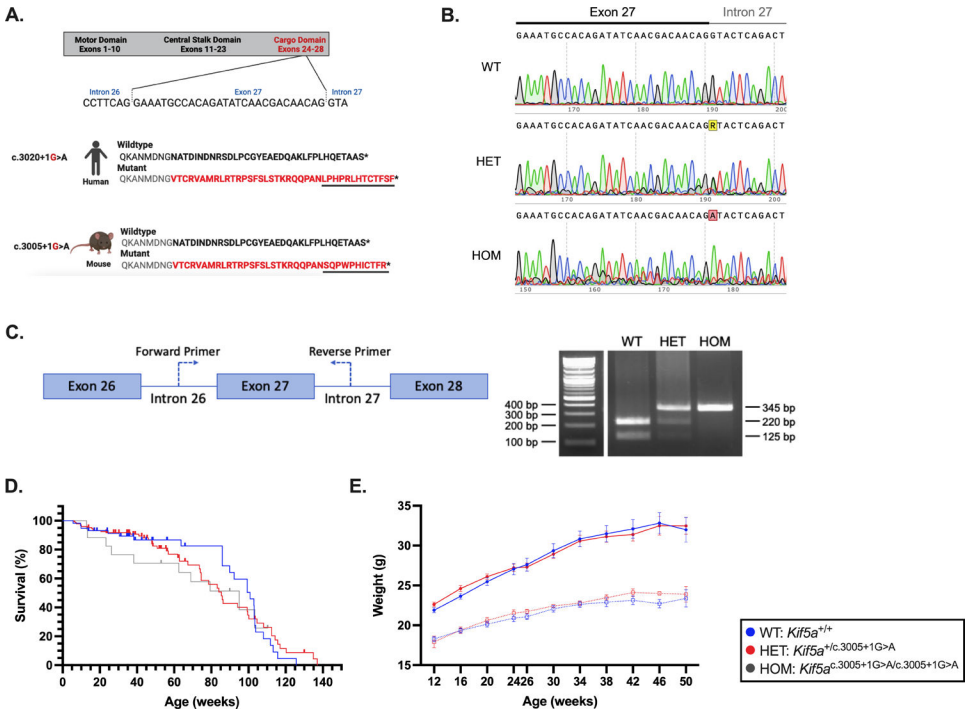

Figure 1. Generation of *Kif5a*$^{c.3005+1G>A}$ mouse

A. Point mutation c.3005+1 G>A at the 3' exon 27 splice junction was introduced using CRISPR-Cas9. The gRNA sequence followed by PAM was also part of the genetically edited site conserved in human and mouse. The mutation introduced is predicted to have a novel KIF5A C-terminal only 13 amino acids different from the human counterpart.

B. Sanger sequence chromatograms for WT, HET and HOM animals. In the HET chromatograph, "R" represents the base A or G.

C. RT-PCR and Rsa1 restriction confirmed the loss of exon 27 in mRNAs from HET mice. Sample genotyping results shown.

D. Survival of HET and HOM mice was comparable to WT mice in a 36-month analysis (Blue: WT n=68; Red: HET n=142; Gray: HOM n=50, p=0.835).

E. Weight evaluation showed no difference between WT (blue) versus HET (red), with males (closed circles) of both genotypes weighing more than the females (open circles). n≥10 per sex per group.

Blue = WT; Red = HET; Black = HOM.

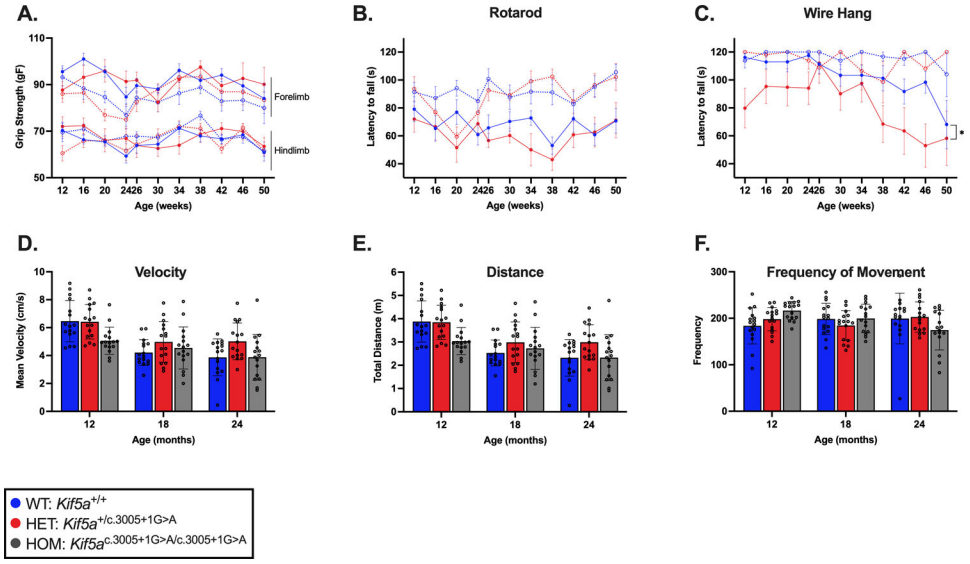

Figure 2. Behavior assessments and electrophysiology studies do not reveal major phenotypic differences between WT and *Kif5a* mutant mice

A. Bilateral grip strength of HET mice, in both males (closed circles) and females (open circles), were similar to WT mice. Forty-seven WT and HET mice matched by age, sex, genotype, and founder line were included in the longitudinal behavioral study (WT male, n=14; WT female, n=12; HET male, n=11; HET female, n=10), used for grip strength (results reported in gram-force [gF]; **A**), rotarod (**B**) and wire hang (**C**).

B-C. Males performed worse in both rotarod and wire hang tests. Male HET mice had a mildly decreased wire hang performance at 1 year.

D-F. Open field measures (velocity, total distance traveled, and frequency of movement) were comparable between genotypes. N=8 per genotype per sex at all timepoints. One-way ANOVA; * $p<0.05$. Blue=WT; Red=HET; Black=HOM.

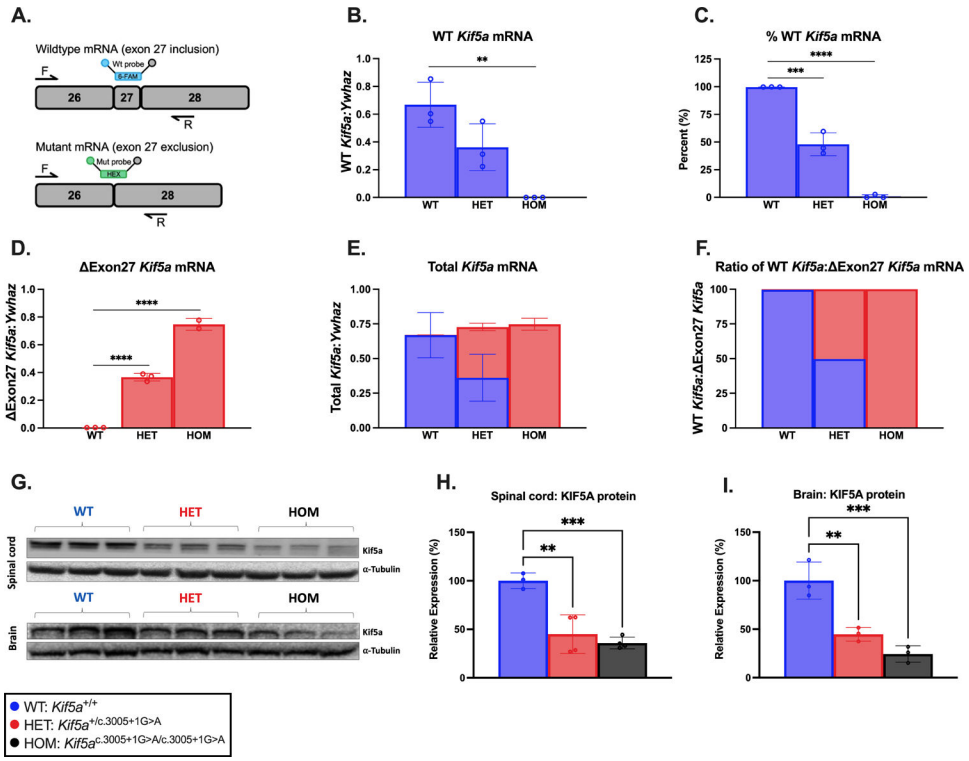

Figure 3. *Kif5a* mRNA and Protein Analysis across genotypes.

A. Assays were designed to detect WT and Δexon27 *Kif5a* mRNA expression via ddPCR. Results were normalized to the ubiquitously-expressed gene *Ywhaz*.

B. Concentration of WT *Kif5a* mRNA decreased from WT to HOM mice.

C. WT *Kif5a* mRNA levels in WT, HET and HOM mice neuronal tissue (B) and % WT *Kif5a* (C).

Percent of WT *Kif5a* mRNA (WT mice normalized to 100%), progressively declined in HET and HOM mice.

D. The concentration of ΔExon27 *Kif5a* mRNA level significantly increased in both HET and HOM mice compared to WT.

E-F. WT (blue) and Δexon27 (red) *Kif5a* mRNA levels are shown together, across all genotypes, displayed as total mRNA levels (E) and fraction of total levels as a percent (F).

G-I. Representative western blot image (G) for spinal cord and brain protein quantification. Total Kif5a protein levels in spinal cord (H) and brain (I) are decreased in HET and HOM mice as compared to WT.

Blue = WT *Kif5a* mRNA, red = ΔExon27 *Kif5a* mRNA (panels A-F); Blue = WT, Red = HET, Black = HOM (panels G-I); n=3 per genotype. Unpaired t-test and One-Way ANOVA test; ** $p<0.01$, *** $p<0.001$, **** $p<0.0001$.

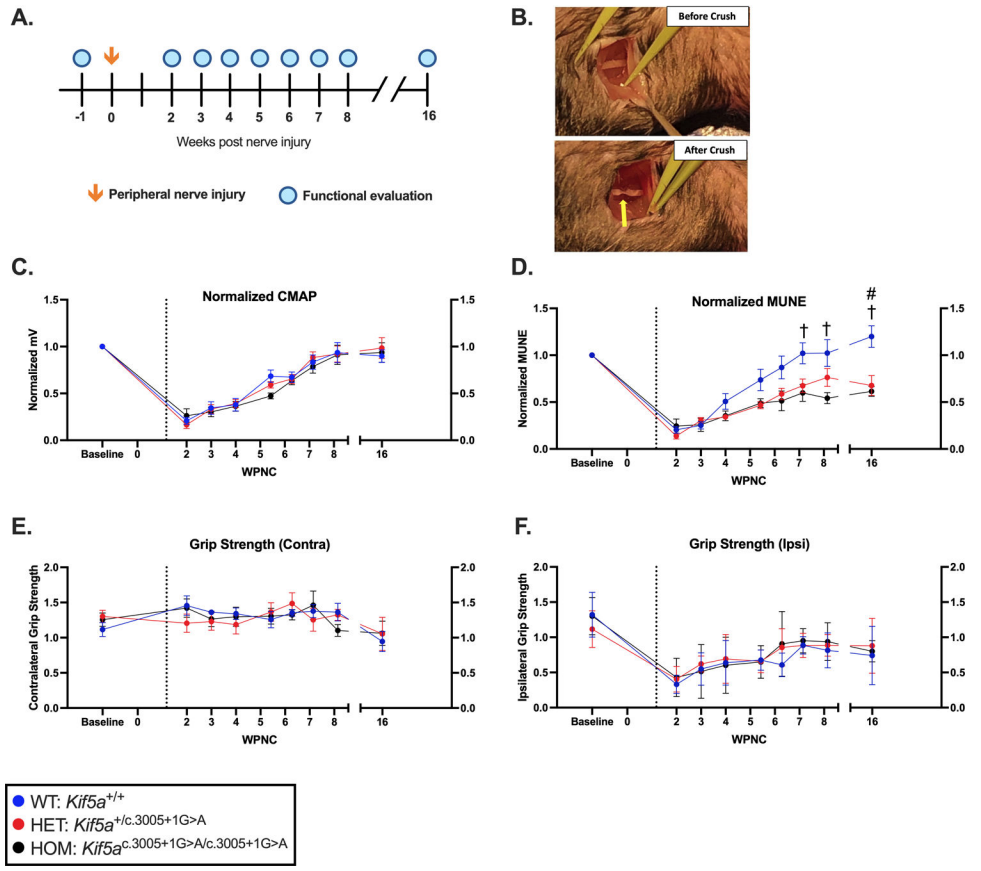

Figure 4. Electrophysiological recovery after PNI showed delayed MUNE recovery.

A. Timeline for functional evaluations prior to and following PNI, including pathological evaluation.

B. Visual of crush procedure. A small incision is made on the medial aspect of the right leg, and hemostatic forceps were used to crush the sciatic nerve while maintaining the axoplasm.

C. No differences in CMAP were observed at final timepoint or during recovery.

D. Delayed and incomplete MUNE in was observed in mutant mice at 16 weeks post PNI.

E-F. No differences in grip strength were observed on the uninjured (left, contralateral) leg or the injured (right, ipsilateral) leg. Grip recordings were normalized to mouse weight at the time of the evaluation.

N=8 per genotype. One-way ANOVA with Kruskall-Wallis test. $p<0.05$ *, $p<0.01$ **. Blue = WT; Red = HET; Black = HOM. WPNC = weeks post nerve crush.

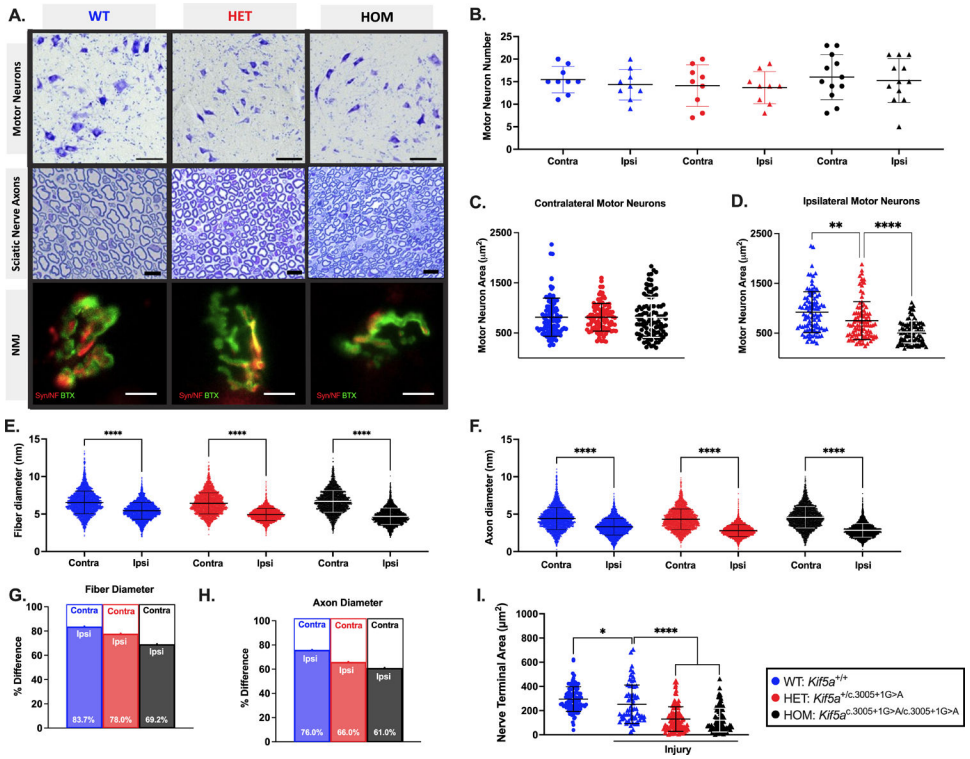

Figure 5. Pathological correlates in multiple motor unit tissues of injured mutant *Kif5a* mice.

A. Representative images of ipsilateral WT, HET, and HOM lumbar spinal cord motor neurons, sciatic nerve cross-sections 5mm distal to injury site, and gastrocnemius NMJs. Scale bars: motor neurons=50μm; axons=10μm; NMJs=5μm.

B-D. Lumbar motor neuron analysis of the contralateral and ipsilateral sciatic motor neuron pool demonstrated reduced motor neuron area (**C-D**) without loss of motor neurons (**B**).

E-H. Ipsilateral fiber (E) and axon (F) diameters decreased across all genotypes compared to uninjured (contra) sciatic nerves. When assessing the difference (ipsilateral divided by contralateral expressed as a percentage), HOM mice showed the greatest reduction in fiber (G) and axon (H) diameter after PNI, followed by HET, followed by WT.

I. Injured *Kif5a* mutants exhibited smaller nerve terminal size compared to injured WT mice.

Blue = WT; Red = HET; Black = HOM; n=3 per genotype. One-way ANOVA with Kruskal-Wallis test; $p<0.05$*, $p<0.01$**, $p<0.0001$ ****.

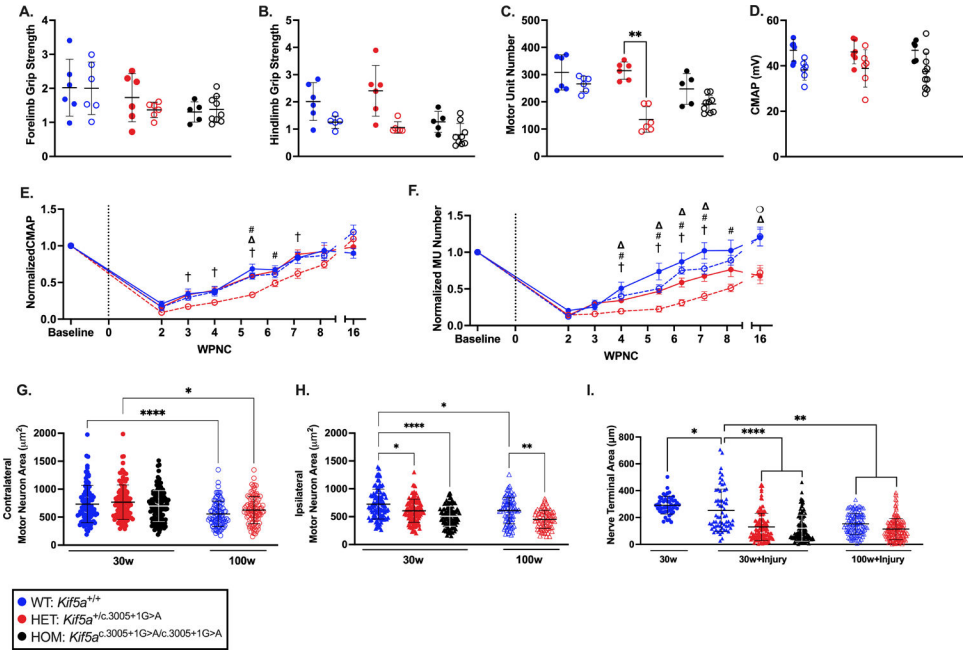

Figure 6. Functional and pathological assessment of aged *Kif5a* mice reveals decline in motor unit maintenance and repair

A-D. Mice were compared at adult (1-year; solid circles) and aged (2-year; open circles) timepoints for each genotype. Forelimb (A) and hindlimb (B) grip strength were not affected by age, nor was CMAP (D), regardless of genotype. However, MUNE (C) decreased with age in HET mice. Grip recordings were normalized to mouse weight at the time of the evaluation.

E-F. Longitudinal recovery was charted across genotypes following PNI at 35w. CMAP recovery (E; normalized to baseline) was slightly delayed in aged HET mice. Between 2–8 WPNC, MUNE recovery deficit (F) in adult HET mice was similar to that in aged WT mice, and both were delayed compared to recovery in adult WT mice. Aged HET mice showed the most dramatic delay in MUNE recovery after PNI. † symbols denote timepoints in which HET mice injured at 35w were significantly different than WT mice injured at 14w. # symbols denote timepoints in which HET mice injured at 35w were significantly different than WT mice injured at 35w. **Δ** symbols denote timepoints in which WT mice injured at 14w were significantly different than HET mice injured at 35w. ❍ symbols denote timepoints in which WT mice injured at 14w were significantly different than HET mice injured at 14w.

G. Contralateral motor neuron area was decreased in injured aged PNI mice (35w at PNI, 100w at euthanasia) compared with injured adult mice (14w at PNI, 30w at euthanasia) but did not differ between genotypes.

H. Ipsilateral motor neuron area in aged WT PNI mice was significantly greater than that of aged HET PNI mice but did not differ from adult HET PNI mice.

I. Nerve terminal area decreased in injured aged PNI mice but did not differ between genotypes or differ with injured adult HET and HOM mice.

N=6–8 mixed sex for all cross-sectional in vivo experiments (A-D), only male mice were used for aged longitudinal PNI recovery (E-F, n>8 per genotype); pathological analyses

were performed on n=3 mice per genotype: circles=contralateral, triangles=ipsilateral; closed=adult/30w, open=aged/100w (G-I). One-way ANOVA with Kruskal-Wallis test; $p<0.05$*, $p<0.01$**, $p<0.0001$****.